JOURNAL OF GUIDANCE, CONTROL, AND DYNAMICS
Vol. 30, No. 5, September–October 2007

Digital Autoland Control Laws Using Quantitative Feedback Theory and Direct Digital Design

Thomas Wagner* and John Valasek†
Texas A&M University, College Station, Texas 77843-3141

DOI: 10.2514/1.27761

Autoland controllers are prevalent for both large and small/micro unmanned aerial vehicles, but very few are available for medium-sized unmanned air vehicles. These vehicles tend to have limited sensors and instrumentation, yet must possess good performance in the presence of modeling uncertainties and exogenous inputs such as turbulence. Quantitative feedback theory has been reported in the literature for inner-loop control of several aircraft problems, but not for outer-loop control or for automatic landing. This paper describes the synthesis and development of an automatic landing controller for medium-sized unmanned aerial vehicles, using discrete quantitative feedback theory. Controllers for the localizer, glideslope tracker, and automatic flare are developed, with a focus on outer-loop synthesis and robustness with respect to model uncertainty. Linear, non-real-time, six-degree-of-freedom Monte Carlo simulation is used to compare the quantitative feedback theory controller with a baseline proportional–integral controller in several still-air and turbulent-air landing scenarios. Results presented in the paper show that the quantitative feedback theory controller provides superior performance robustness to the proportional–integral controller in turbulent-air conditions when model uncertainties are present. It is therefore concluded to be a promising candidate for an autoland controller for unmanned air vehicles.

Nomenclature

A	=	plant matrix
AR	=	aircraft aspect ratio
B	=	control distribution matrix
b	=	aircraft wingspan
C	=	output matrix, coefficient
c	=	mean aerodynamic chord
D	=	carry-through matrix
d	=	distance
F	=	prefilter transfer function
G	=	controller transfer function
GM	=	gain margin
h	=	altitude
K	=	gain
L	=	loop transfer function
$\boldsymbol{P}$	=	set of plant transfer functions
PM	=	phase margin
p	=	aircraft body-axis roll rate
q	=	aircraft body-axis pitch rate
r	=	aircraft body-axis yaw rate, transfer function reference input
R	=	slant range to runway
SM	=	stability margin
s	=	Laplace variable
T	=	sample period, closed-loop transfer function
t	=	aircraft airfoil thickness
u	=	aircraft total velocity
$\boldsymbol{u}$	=	control vector
$\boldsymbol{x}$	=	state vector
y	=	transfer function output
$\boldsymbol{y}$	=	output vector
z	=	discrete z-transform variable
α	=	angle of attack
β	=	sideslip angle
δ	=	control deflection
θ	=	aircraft body-axis pitch attitude angle
Λ	=	wing sweep angle
ζ	=	damping ratio
τ	=	time constant
ϕ	=	aircraft body-axis roll attitude angle
ω	=	frequency

Thomas Wagner graduated magna cum laude with a B.S. degree in aerospace engineering (2004) and an M.S. degree in aerospace engineering (2006), both from Texas A&M University. He interned for two summers at S-TEC Corporation working as a test pilot and a test engineer on autopilot systems for high-performance General Aviation aircraft. From 2004 to 2006, he worked as a graduate research assistant in the Flight Simulation Laboratory at Texas A&M University, researching digital flight control and automatic landing systems, as well as autonomous aerial refueling. In 2006, he served as the lead research pilot for the Flight Simulation Laboratory at Texas A&M University. He is currently a 2nd lieutenant and pilot candidate in the U.S. Air Force. He is a Member of AIAA.

A biography of John Valasek appears in Vol. 29, No. 4.

Presented as Paper 6599 at the AIAA Guidance, Navigation, and Control Conference, Keystone, CO, 21–24 August 2006; received 11 September 2006; revision received 7 April 2007; accepted for publication 10 April 2007.

*Graduate Research Assistant, Flight Simulation Laboratory, Aerospace Engineering Department; twwagner@tamu.edu. Student Member AIAA.
†Associate Professor and Director, Flight Simulation Laboratory, Aerospace Engineering Departments; valasek@tamu.edu. Associate Fellow AIAA.

Subscripts

A	=	airspeed
c	=	commanded
$c/2$	=	midchord
D	=	drag force, disturbance
dr	=	Dutch roll
eff	=	effective aspect ratio
F	=	flare
fb	=	feedback
GS	=	glideslope
IGE	=	in-ground effect
L	=	lift force, lower limit
LOC	=	localizer
l	=	rolling moment
m	=	pitching moment
n	=	yawing moment
OGE	=	out-of-ground effect
R	=	tracking
sprl	=	spiral
U	=	upper limit
Y	=	side force
θ	=	pitch attitude
ψ	=	heading
0	=	zero lift, nominal case

I. Introduction

THE landing phase of flight presents unique challenges to designing a flight control system for the approach and touchdown of an aircraft. Atmospheric disturbances such as wind and turbulence require a controller to reject external disturbances introduced to the system. Because of preliminary modeling limitations, parameter uncertainties are present in a system, and the controller must be insensitive to these uncertainties. In addition to parameter insensitivity and disturbance rejection, an autoland controller must provide an accurate approach and smooth touchdown to prevent damage to the aircraft. Although this research is for unmanned aerial vehicles, the work and results found from this paper apply for piloted aircraft as well. The techniques developed in this paper can easily be extended to general aviation aircraft, military aircraft, or commercial aircraft.

For any automatic landing system, regardless of the control methodology used, the following requirements must be met:

1) Provide good performance during approach and landing for a safe touchdown without damage.

2) Offer robustness to model uncertainties and external disturbances such as wind and turbulence.

3) Give repeatable results for a variety of possible aircraft configurations and environmental conditions.

The autoland problem has been successfully approached by a variety of methods. References [1,2] used proportional–integral (PI) controllers for the automatic landing of large transport aircraft. Fuzzy logic has been used to solve the autoland problem for a medium-sized transport aircraft in [3], and neural networks have been used for a large transport aircraft in [4]. Mixed H_2/H_∞ control was applied to the automatic landing of an F-14 aircraft in [5]. All of the aforementioned techniques were applied to larger manned vehicles. Reference [6] applied the linear-quadratic technique to the automatic landing of a small unmanned aerial vehicle (UAV), and [7] develops a fault-tolerant automatic landing controller for the Heron UAV, which is a medium-sized UAV. Several autoland systems exist for small or micro UAVs,[‡] and vehicle specific controllers exist for the automatic landing of large UAVs [8–10]. Very few systems are available for medium-sized UAVs. Sierra Nevada Corporation offers an automatic landing system for medium-sized UAVs, but this system is expensive and requires additional ground equipment.[§]

[‡]Data available online for the Piccolo autopilot at www.cloudcaptech.com and for the Kestrel autopilot at www.procerusuav.com [retrieved July 2006].

[§]Data available online for the millimeter-wave beacon tracking system at http://www.sncorp.com/prod/atc/uav/uav1.shtml [retrieved July 2006].

Quantitative feedback theory (QFT) is a design technique that offers robust performance amidst structured model uncertainties. This technique can be applied to multiple-input, single-output (MISO) systems and multiple-input, multiple-output (MIMO) systems in both the time and frequency domains [11,12]. QFT has been successfully applied to a number of vehicles, both manned and unmanned. QFT was used for inner-loop stability control of various aircraft such as the F-15, F-16, and X-29 [13]. A pitch attitude hold controller was developed for both a fighter jet and a business jet in [14], and a lateral/directional flight control system was designed in [15] for a large transport aircraft. Reference [16] documents the first flight test of a QFT longitudinal controller on a small UAV, and [17] documents the design and flight test of a QFT pitch rate stability augmentation system for a small UAV.

Most research to date in QFT has focused on inner-loop flight control, with little or no work on synthesis of the outer loops. The unique specific contributions of this paper are the development of a QFT controller using direct digital design for the approach and automatic landing of a medium-sized UAV and detailing of the synthesis and interactions of the outer loops. Performance of the digital QFT controller is quantified by Monte Carlo simulation comparison with a baseline PI approach and automatic landing controller. A detailed parametric study on the effect of model uncertainties, turbulence, and winds is also presented.

The paper is organized as follows. Section II introduces and details the specifics of the approach and landing problem. Section III describes the development of a nonparametric aircraft model using system identification and verifies the identified model. Section IV presents the digital controller synthesis, describing the development of the QFT and PI controllers. Finally, simulation results are reported in Sec. V, and conclusions are presented in Sec. VI.

II. Problem Statement and Definition

The purpose of this section is to describe the approach and landing problem posed for this research. As noted in Sec. I, the automatic landing consists of intercepting a lateral and vertical beam and tracking the guidance provided to a specified height above the runway, at which time a flare maneuver is performed. It is assumed that a guidance system is available to provide lateral and vertical guidance to the start of the flare. Figure 1 details the geometry used to determine deviations from the lateral and vertical beam, and Fig. 2 illustrates the geometry of the flare maneuver. A category (CAT) IIIc (no requirements on cloud ceiling or visibility) instrument landing system (ILS) is assumed for this paper, although the techniques can easily be extended to any guidance system that provides precision guidance data. Because ILS is assumed, the lateral beam will be referred to as the localizer, and the vertical beam will be referred to as the glideslope.

The localizer consists of a transmitter stationed at the far end of the runway, which sends out a signal that is approximately 5 deg wide (beam width) and is centered on the runway centerline. Typical interception occurs when the aircraft flies at a heading to intercept the localizer at a range of 6–10 n mile from the runway threshold. The glideslope consists of a transmitter stationed approximately 1000 ft from the approach end of the runway, which sends a beam that is elevated approximately 3 deg above the horizon and approximately 1.4 deg wide. The glideslope is intercepted by flying straight and level at a specified altitude until flying through the beam at a range of 4–5 n mile from the runway threshold, at which time the beam is tracked down to the flare height [18].

Another component in the automatic flare system is the airspeed command and hold, which controls the airspeed of the aircraft using the throttle. During the approach, the airspeed is maintained at the specified approach speed, and after passing through the flare height, the airspeed is reduced to just above the stall speed before touchdown. If airspeed is not properly maintained, the aircraft will have difficulty tracking the glideslope, and during the flare, the aircraft will either float down the runway or land with a higher velocity than normal, which could damage the aircraft.

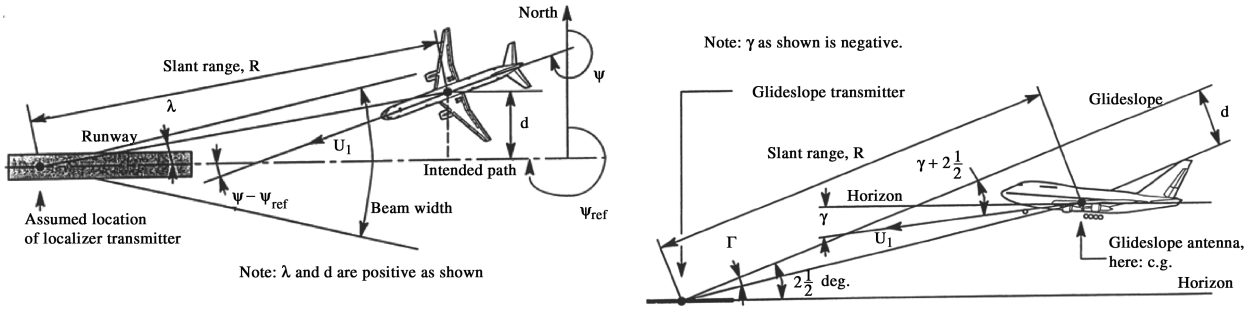

Fig. 1 Localizer and glideslope tracking geometry [19].

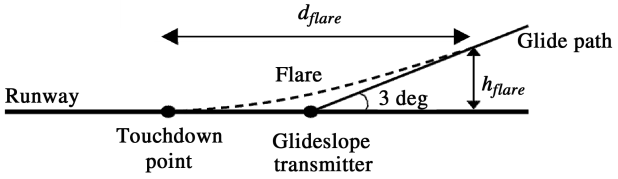

Fig. 2 Autoflare geometry.

To provide a smooth transition from the flare height to the runway, an exponential function is given as a reference trajectory, which has the form shown in the following equation.

$$\dot{h} = h_{\text{flare}} e^{-\frac{1}{\tau}} \tag{1}$$

In the preceding equation, h_{flare} is the height at which the flare maneuver is started, and τ is a time constant used to shape the trajectory. Following the method of [1], the trajectory was shaped for a touchdown point 1000 ft beyond the start of the flare, which leads to $\tau = 1.99$ s, and $h_{\text{flare}} = 17.47$ ft. This is reasonable for an aircraft of this size, because most general aviation aircraft start to flare between 10 and 30 ft above the ground.

It is desired for the aircraft to intercept the localizer and glideslope and track these beams to the runway centerline and to the flare height. After reaching the flare height, the vehicle should touch down with a small vertical velocity to prevent damage to the aircraft, and it is also desired to minimize the distance traveled down the runway to prevent running off the runway. Reference [19] states that damage occurs at a touchdown velocity of greater than 10 ft/s and "hard" landings occur at a touchdown velocity of greater than 6 ft/s. Additional considerations should be made to ensure that the pitch attitude angle is greater than the nominal pitch attitude angle when the aircraft is resting on the ground to prevent "wheelbarrowing" or landing on the nose gear first.

III. Aircraft Model

The nonparametric aircraft model used for synthesis and simulation of the approach and flare control laws was derived using system identification of a real-time, high-fidelity, nonlinear six-degree-of-freedom flight simulator. The simulation model is a Rockwell Commander 700, a light twin-engine general aviation aircraft.

Although this vehicle is much larger than a medium-sized UAV, it is assumed here that the dynamics of this vehicle are generally representative of those of a medium-sized UAV. Because a high-fidelity nonlinear model exists, observer/Kalman filter identification (OKID) [20] is used to determine a linear time-invariant (LTI) state-space representation of the C700. The linear state-space model is in the form

State equation:

$$\dot{\boldsymbol{x}} = A\boldsymbol{x} + B\boldsymbol{u} \tag{2a}$$

Output equation:

$$\boldsymbol{y} = C\boldsymbol{x} + D\boldsymbol{u} \tag{2b}$$

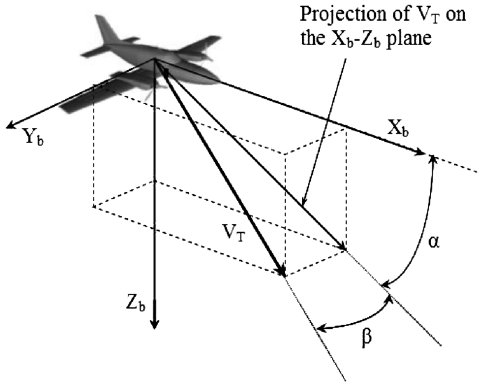

Fig. 3 Definition of body-axis system and aerodynamic angles.

where the state vector $\boldsymbol{x} \in R^{n\times 1}$ has n states, control vector $\boldsymbol{u} \in R^{m\times 1}$ has m inputs, output vector $\boldsymbol{y} \in R^{p\times 1}$ has p outputs, the plant matrix $A \in R^{n\times n}$, control distribution matrix $B \in R^{n\times m}$, and $C \in R^{p\times n}$ and $D \in R^{p\times m}$ are matrices that determine the elements of the output vector. The dynamic models are expressed in the stability axis system, which is depicted in Fig. 3.

For the identification effort, the aircraft was in the power-approach configuration (gear down, flaps down) at the flight condition listed in Table 1 [21].

A. Lateral/Directional Model

The states of the lateral/directional model are sideslip angle β, body-axis roll rate p, body-axis yaw rate r, and body-axis roll attitude angle ϕ. Aileron deflection δ_a and rudder deflection δ_r are the lateral/directional controls. A 3-2-1-1 aileron maneuver followed immediately by a 3-2-1-1 rudder maneuver was used to perturb the lateral/directional model. The 3-2-1-1 maneuver involves a series of control inputs in which the control is commanded to one side for 3 s, the opposite side for 2 s, and finally, a 1-s control input in each direction. The identified lateral/directional model is shown in the Appendix.

The eigenvalues and modes of the lateral/directional system are

$$\begin{aligned} &\lambda_{\text{dr}} = -0.312 \pm 1.92i \qquad \lambda_{\text{roll}} = -2.02 \qquad \lambda_{\text{sprl}} = 0.0067 \\ &\zeta_{\text{dr}} = 0.160 \qquad T_{\text{roll}} = 0.50 \text{ s} \qquad T_{\text{sprl}} = -149 \text{ sec} \\ &\omega_{n_{\text{dr}}} = 1.95 \text{ rad/s} \end{aligned} \tag{3}$$

Table 1 C700 power-approach flight condition

Parameter	Value	Units
Altitude, h_1	1000	ft
Airspeed, U_1	151.9	ft/s
Pitch attitude, θ_1	0.66	deg
Angle of attack, α_1	0.65	deg
Elevator deflection, δ_{e_1}	1.996	deg
Throttle setting, δ_{T_1}	75.26	%

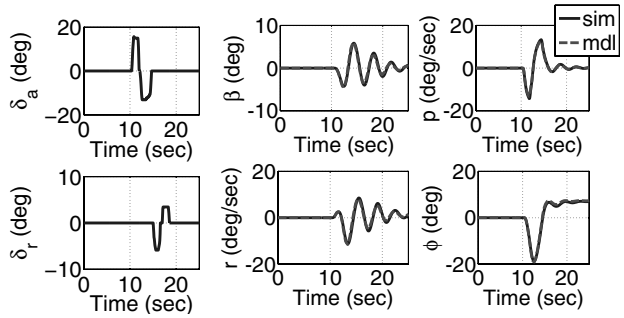

Fig. 4 Lateral/directional model verification.

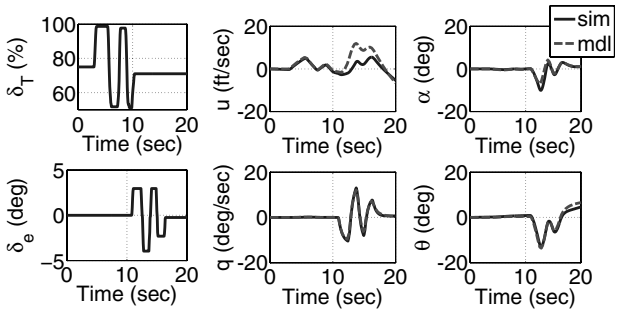

Fig. 5 Longitudinal model verification.

The model exhibits standard modes, with an unstable spiral mode. This is not a great concern because many aircraft have an unstable spiral mode and this instability is often stabilized using feedback.

The identified model is verified with the nonlinear simulator model using different inputs than were used for the identification maneuver. Because a 3-2-1-1 input was given for the original identification, an aileron doublet was introduced followed by a rudder doublet. The lateral/directional verification plots of Fig. 4 show that the identified model compares well with the nonlinear simulator model for all states. It is concluded that the identified model is representative of the actual dynamics of the simulator. Finally, a first-order actuator model with a time constant of $\tau = 0.1$ s is assumed for the aileron and rudder.

$$\frac{\delta}{\delta_c}(s) = \frac{1/\tau}{s + 1/\tau} \tag{4}$$

B. Longitudinal Model

The longitudinal model was identified in the same manner as the lateral/directional model described earlier. The perturbed states of the longitudinal state-space model are aircraft total velocity u, angle of attack α, body-axis pitch rate q, and pitch attitude angle θ. A throttle doublet followed by an elevator doublet was used to identify the longitudinal model. The identified longitudinal model found from OKID is shown in the Appendix.

The dynamic modes and eigenvalues of the longitudinal model are

$$\begin{aligned} &\lambda_{3\text{rd}} = -0.138 \pm 0.136i \qquad \lambda_3 = -0.861 \qquad \lambda_4 = -2.24 \\ &\zeta_{3\text{rd}} = 0.712 \qquad T_3 = 1.16 \text{ s} \qquad T_4 = 0.45 \text{ s} \\ &\omega_{n_{3\text{rd}}} = 0.194 \text{ rad/s} \end{aligned} \tag{5}$$

The dynamic modes show that this system has a third oscillatory mode and two first-order stable modes. Although not standard for aircraft, the third oscillatory mode usually does not present a problem for control law design. Because doublets were used to identify the longitudinal model, a 3-2-1-1 throttle input was followed by a 3-2-1-1 elevator input. Figure 5 displays the verification of the identified longitudinal model and shows that it agrees well with the simulator dynamics. Although frequency content matches well, the amplitude does not, because there is a discrepancy in airspeed between 10 and 20 s. This difference is not of great concern because the airspeed will be controlled by the throttle, and during the time period in which a throttle input is applied to the system, airspeed matches well in both frequency and amplitude. A first-order actuator model is assumed for the elevator and throttle dynamics. The elevator was assumed to have a 0.1-s time constant, the throttle was modeled with a 0.33-s time constant, and the engine was modeled with a lag of 1 s.

C. Ground-Effect Modeling

As the aircraft descends toward the ground, the trailing edge vortex development is disrupted by the ground, which tends to increase the upwash on the wing surface such that the lift coefficient C_L is increased and the induced drag coefficient C_{D_i} is decreased. It is assumed that the decrease in drag is small, and thus the focus of the ground effect modeling will be centered on the increase in lift. This increase in lift can be viewed as an increase in the aircraft lift curve slope C_{L_α} and a decrease in the zero-lift angle of attack α_0. From [22], the change in α_0 can be approximated by Eq. (6).

$$\Delta\alpha_0 = \frac{t}{c}\left[-0.1177\frac{1}{(h/c)^2} + 3.5655\frac{1}{(h/c)}\right] \tag{6}$$

In Eq. (6), t/c is the thickness ratio of the aircraft, and h/c is the aircraft height above the ground normalized by the mean aerodynamic chord. The increase in C_{L_α} can be expressed as in Eq. (7).

$$C_{L_{\alpha_{\text{IGE}}}} = \frac{2\pi AR_{\text{eff}}}{2 + \sqrt{AR_{\text{eff}}^2(1 + \tan^2\Lambda_{c/2}) + 4}} \tag{7}$$

In Eq. (7), $\Lambda_{c/2}$ is the midchord sweep angle and AR_{eff} is the effective aspect ratio, which can be approximated by

$$\begin{aligned} \frac{AR}{AR_{\text{eff}}} = &-0.0235\left(2\frac{h}{b}\right)^6 + 0.2803\left(2\frac{h}{b}\right)^5 - 1.2428\left(2\frac{h}{b}\right)^4 \\ &+ 2.7442\left(2\frac{h}{b}\right)^3 - 3.3818\left(2\frac{h}{b}\right)^2 + 2.447\left(2\frac{h}{b}\right) + 0.096 \end{aligned} \tag{8}$$

where the independent variable is the aircraft height above the ground normalized by the wingspan of the aircraft. To analyze the robustness of the control laws to turbulence, the Dryden wind turbulence block of the MATLAB aerospace block set is incorporated in the simulation. This model uses the Dryden spectral representation to add turbulence to the model by passing band-limited white noise through forming filters, as defined in [23]. The turbulence is then added as an exogenous input to the aircraft model.

D. Model Uncertainties

Because the identified nonparametric linear models developed earlier do not indicate where particular uncertainties appear in the model, stability and control derivatives were used to construct a parametric state-space model according to the linearized equations of motion, using Taylor series expansions. Assuming that the longitudinal and lateral/directional dynamics are decoupled, which is the case for $\phi = 0$, the linearized equations of motion for both the lateral/directional and longitudinal axes take the form shown in Eqs. (9) and (10), respectively.

Table 2 Lateral/directional stability derivative uncertainty [24]

Derivative	Importance	Accuracy, ±%
C_{y_β}	7	20
C_{l_β}	10	20
C_{n_β}	10	15
C_{y_p}	4	50
C_{l_p}	10	15
C_{n_p}	8	90
C_{y_r}	4	30
C_{l_r}	7	40
C_{n_r}	9	25

$$\begin{bmatrix} 1 & 0 & 0 & 0 \\ 0 & 1 & -\frac{I_{xz}}{I_{xx}} & 0 \\ 0 & -\frac{I_{xz}}{I_{zz}} & 1 & 0 \\ 0 & 0 & 0 & 1 \end{bmatrix} \begin{bmatrix} \dot{\beta} \\ \dot{p} \\ \dot{r} \\ \dot{\phi} \end{bmatrix} = \begin{bmatrix} \frac{Y_\beta}{U_1} & \frac{Y_p}{U_1} & \frac{Y_r}{U_1}+1 & \frac{g\cos(\theta_1)}{U_1} \\ L_\beta & L_p & L_r & 0 \\ N_\beta + N_{T_\beta} & N_p & N_r & 0 \\ 0 & 1 & \tan(\theta_1) & 0 \end{bmatrix} \begin{bmatrix} \beta \\ p \\ r \\ \phi \end{bmatrix} + \begin{bmatrix} \frac{Y_{\delta_a}}{U_1} & \frac{Y_{\delta_r}}{U_1} \\ L_{\delta_a} & L_{\delta_r} \\ N_{\delta_a} & N_{\delta_r} \\ 0 & 0 \end{bmatrix} \begin{bmatrix} \delta_a \\ \delta_r \end{bmatrix} \tag{9}$$

Each term on the right-hand side of Eq. (9) is a dimensional stability derivative associated with a corresponding nondimensional stability derivative. For example, N_β is a function of C_{n_β} and Y_{δ_r} is a function of $C_{y_{\delta_r}}$. Table 2 outlines the relative importance of each stability derivative, with a rating of 10 being the most important and a rating of 1 being the least important. The accuracy to which each derivative can be predicted using preliminary modeling techniques is also given.

Similar data are not readily available for the control power derivatives. Because the lateral/directional controller is based on the roll angle, which is found from the roll rate, the important control derivative for the autoland problem is $C_{l_{\delta_a}}$. The uncertainty in $C_{l_{\delta_a}}$ was arbitrarily chosen to be 25%.

The state-space form of the linearized longitudinal equations of motion are shown in Eq. (10).

$$\begin{bmatrix} 1 & -X_{\dot{\alpha}} & 0 & 0 \\ 0 & 1-\frac{Z_{\dot{\alpha}}}{U_1} & 0 & 0 \\ 0 & -M_{\dot{\alpha}} & 1 & 0 \\ 0 & 0 & 0 & 1 \end{bmatrix} \begin{bmatrix} \dot{u} \\ \dot{\alpha} \\ \dot{q} \\ \dot{\theta} \end{bmatrix} = \begin{bmatrix} X_u + X_{T_u} & X_\alpha & X_q & -g\cos(\theta_1) \\ \frac{Z_u}{U_1} & \frac{Z_\alpha}{U_1} & \frac{Z_q}{U_1}+1 & -\frac{g\sin(\theta_1)}{U_1} \\ M_u + M_{T_u} & M_\alpha + M_{T_\alpha} & M_q & 0 \\ 0 & 0 & 1 & 0 \end{bmatrix} \begin{bmatrix} u \\ \alpha \\ q \\ \theta \end{bmatrix} + \begin{bmatrix} \frac{X_{\delta_e}}{U_1} & \frac{X_{\delta_T}}{U_1} \\ Z_{\delta_e} & Z_{\delta_T} \\ M_{\delta_e} & M_{\delta_T} \\ 0 & 0 \end{bmatrix} \begin{bmatrix} \delta_e \\ \delta_T \end{bmatrix} \tag{10}$$

Table 3 Longitudinal stability derivative uncertainty [24]

Derivative	Importance	Accuracy, ±%
C_{L_α}	10	5
C_{m_α}	10	10
C_{D_α}	5	10
C_{L_u}	4	20
C_{m_u}	7	20
C_{D_u}	1	20
C_{L_q}	3	20
C_{m_q}	9	20
C_{D_q}	1	20

The parameters on the right-hand side of Eq. (10) are dimensional stability derivatives, each of which corresponds to a specific nondimensional stability derivative. For instance, M_α is a function of C_{m_α} and M_{δ_e} is a function of $C_{m_{\delta_e}}$. Table 3 displays the relative importance of each longitudinal derivative and the accuracy to which it can be estimated using preliminary modeling methods.

Because elevator and throttle are the primary longitudinal controls for this problem, 25% uncertainty is added to both $C_{m_{\delta_e}}$ and to $C_{D_{\delta_T}}$. Ground effect is expressed primarily in C_{L_α}, and because the method for including ground effect is approximate, the uncertainty on C_{L_α} is increased to ±25%.

IV. Digital Controller Synthesis

This section details the synthesis of a digital QFT controller and a digital PI controller and then compares them for the autoland task. The control laws developed here will work with any guidance system, provided precision approach data are available at the start of the flare. Both control law designs use a direct digital design approach for sampled data systems using single-input, single-output (SISO) models for synthesis and MIMO models for simulation and evaluation. MATLAB/Simulink is the tool used for all control law synthesis, simulation, and analysis. Because the controllers are to be implemented on a UAV with assumed limited instrumentation, it is desired to use a slow sampling frequency to avoid a large computational burden. The sampling frequency is first determined according to the Shannon sampling theorem, which states that twice the Nyquist frequency, $\omega_s = 2\omega_N = 4$ rad/s $= 0.62$ Hz, should be used to recover the amplitude content of the signals. To additionally recover the frequency content, the sampling frequency was further increased to $\omega_s = 10$ Hz, which corresponds to a sample period of $T = 0.1$ s [25].

Figure 6 illustrates the general control law structure used, with the actuator and vehicle blocks replaced by inner loops for sequential loop closures. The switches before and after the controller represent the sampling of the signals at sample period T s. A zero-order hold is used for control-signal reconstruction.

Specifications for the control laws are based on standard techniques and the authors' experience in flight testing autopilots. Ramp inputs were used, and by tuning the gains, control positions and rates were limited to be less than ±10 deg and ±15 deg/s, respectively. The control laws should meet the requirements specified in MIL-F-9490D [26], which gives the controller requirements as well as specifying a gain margin of at least 6 dB and a phase margin of at least 45 deg for all control loops. It is assumed here that moderate turbulence will be the worst turbulence encountered, and so the control laws are designed to be performance-robust up to and including moderate turbulence. Robustness of each loop is evaluated with a sigma-Bode plot. The low-frequency specifications used are [27] 1) a large minimum singular value, 2) an attenuation of low-frequency disturbances by a factor of 0.25, 3) a slope of at least −20 dB/decade, 4) a zero steady-state error, 5) a minimum crossover frequency of 0.1 rad/s, and 6) a maximum crossover frequency of 10 rad/s.

The high-frequency specifications used are [27] 1) a small maximum singular value and 2) a linear-model accuracy to within

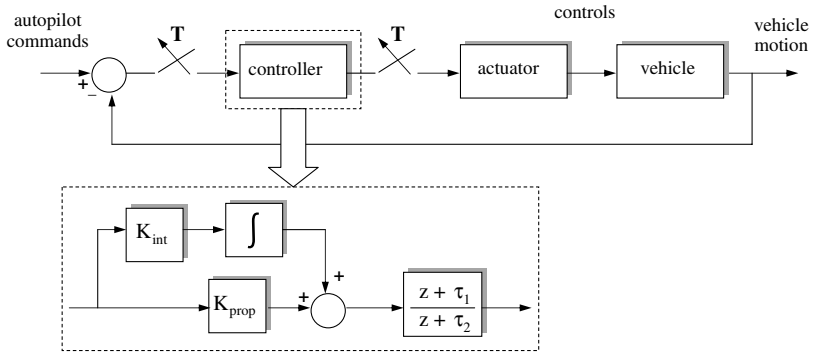

Fig. 6 Control law structure.

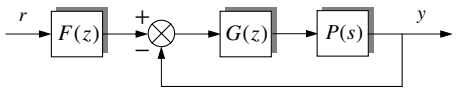

Fig. 7 QFT block diagram.

±10% of the actual plant for frequencies up to 2 rad/s, in which uncertainty grows without bound at 20 dB/decade thereafter.

$$m(\omega) = \frac{s+2}{20} \tag{11}$$

where $m(\omega)$ is the multiplicative modeling discrepancy bound.

A. Quantitative Feedback Theory Controllers

Quantitative feedback theory is a robust control design technique that uses feedback to achieve responses that meet specifications despite structured plant uncertainty and plant disturbances. This technique has been applied to many classes of problems such as SISO, MISO, and MIMO for both continuous and discrete cases. For this work, a SISO system is used with sequential loop closures. Consider the block diagram of Fig. 7. The objective of this design technique is to synthesize $G(z)$ and $F(z)$, such that the output y satisfies the desired performance specifications for a reference input r for all plants in the set $\boldsymbol{P}$.

Procedurally, QFT design can be summarized as follows:

1) Determine the set of plants $\boldsymbol{P}$ that cover the range of structured parameter uncertainty as well as plant templates for each frequency of interest.

2) Specify acceptable tracking models that the closed-loop response satisfies, $T_{R_L} \leq T_R \leq T_{R_U}$, and determine tracking bounds.

3) Determine disturbance rejection models T_D based on disturbance rejection specifications, and determine disturbance bounds.

4) Specify stability margin and determine U contours.

5) Draw U contours, disturbance bounds, and tracking bounds on a Nichols chart.

6) Synthesize nominal loop transfer function $L_0(z)$.

7) Synthesize prefilter $F(z)$.

8) Simulate system to evaluate performance [11].

9) Iterate as required to meet specifications.

Using the preceding list as a guideline, each loop of the autoland system is designed using the QFT technique. When using sequential loop closures with QFT, most of the uncertainty lies in the inner loops of the system. After a suitable controller is designed, outer loops are subject to either the same amount or less uncertainty. Thus design of the outer loops is essentially similar to design of the inner loops. The Terasoft QFT Toolbox in MATLAB is used for creating bounds and synthesizing the QFT control laws.

1. *Lateral/Directional QFT Controller*

Synthesizing the lateral/directional approach control laws involves three sequential loop closures. The innermost loop is bank-angle command and hold, which is closed by a heading command-and-hold loop, which is in turn closed by a localizer tracker loop. Because the handling qualities of this aircraft are open-loop level 1 for the roll and Dutch roll modes, a roll damper and yaw damper are not needed. The bank-angle command-and-hold system is shown in Fig. 8.

The set of plants that cover the range of structured parametric uncertainty was determined using the analysis on model uncertainties in Sec. III. The nominal plant is chosen as the original model found using OKID, without any errors included. The plant templates were determined by plotting the frequency response of every possible combination of stability and control derivative uncertainties and then determining the boundary of all these responses. Six frequencies were used for the design: $\omega = 0.1, 0.5, 2, 5, 15$, and 30 rad/s. The templates obtained using these different frequencies are plotted in Fig. 9.

The tracking models were determined using a set of specifications based on a unit step response, with rise time between 3 and 5 s and overshoot less than 20%. Using this criteria, the transfer functions for T_{R_L} and T_{R_U} shown in Eq. (12) were selected.

$$T_{R_L} = \frac{1.25}{s^2 + s + 0.25} \tag{12a}$$

$$T_{R_U} = \frac{0.6944}{s^2 + 0.7599s + 0.6944} \tag{12b}$$

To help with the design of the prefilter, it is common to add a pole to the lower tracking model and a zero to the upper tracking model. This does not affect the responses, but increases the separation between the upper and lower models on a Bode magnitude plot as the frequency increases [11]. Equation (13) shows the resulting tracking models after adding the additional pole and zero.

$$T_{R_L} = \frac{1.25}{s^3 + 6s^2 + 5.25s + 1.25} \tag{13a}$$

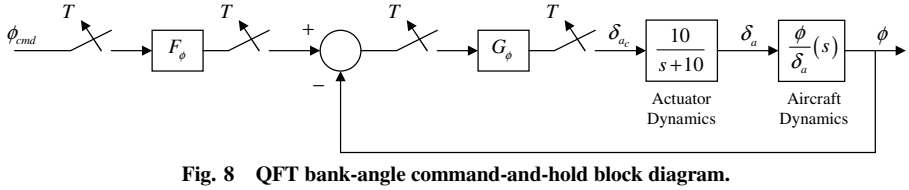

Fig. 8 QFT bank-angle command-and-hold block diagram.

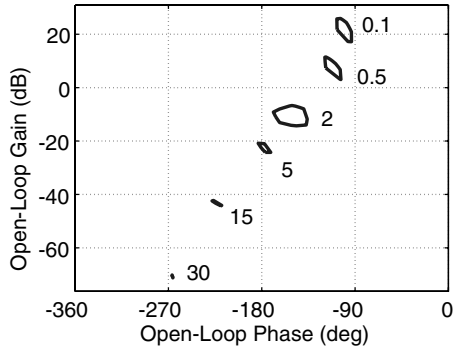

Fig. 9 Bank-angle command-and-hold templates.

$$T_{R_U} = \frac{0.1389s + 0.6944}{s^2 + 0.7599s + 0.6944} \tag{13b}$$

Figure 10 shows the time response of the upper and lower tracking models as well as a Bode magnitude plot for the original models and the augmented models. The original models are plotted as dashed lines and the augmented models are plotted as solid lines. As seen in the figure, augmentation does not significantly affect the time response or the desired specifications, but it does cause the separation between the Bode magnitude plots to increase as frequency is increased, as desired.

For this design, disturbance rejection is not included because satisfying disturbance rejection requirements resulted in large gains that caused control position and rate saturation. Instead, adequate disturbance rejection is provided by meeting the tracking requirements. The stability margin is determined based on the desired gain margin and phase margin for all plants in the set $\boldsymbol{P}$. For this problem a stability margin of 1.2 was used, which leads to $GM = 5.3$ dB and $PM = 49.3$ deg using Eq. (14).

$$GM = 20\log\left(1 + \frac{1}{SM}\right) \tag{14a}$$

$$PM = 180 - \cos^{-1}\left(\frac{0.1}{SM^2} - 1\right) \tag{14b}$$

Using the QFT toolbox, the bounds and stability margins are plotted on a Nichols chart for each frequency value (Fig. 11). Using these bounds, the nominal loop transfer function L_0 should pass below and to the right of the oval bounds (stability bounds) and should lie above the line bounds (tracking bounds) at that specific frequency.

Figure 12 shows the nominal loop transfer function with and without the controller of Eq. (15).

$$G_\phi(z) = \frac{1.0369(z - 0.8484)}{(z - 0.8021)} \tag{15}$$

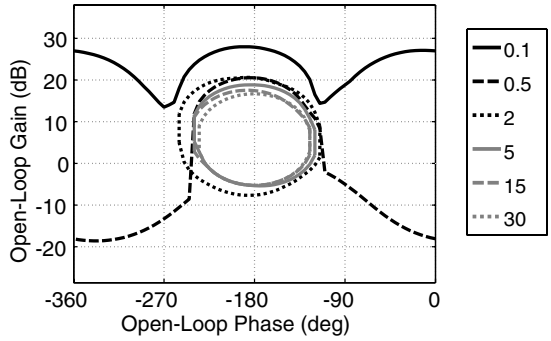

Fig. 11 Bank-angle command-and-hold bounds.

As seen in Fig. 12, the controller $G_\phi(z)$ meets the specifications. The design of the prefilter involves shaping the loop transfer function Bode magnitude plot. Equation (16) displays the prefilter as designed for the bank-angle command-and-hold loop, and Fig. 13 shows the loop transfer function Bode magnitude plot with and without the prefilter.

$$F_\phi(z) = \frac{0.23834(z^2 - 1.692 + 0.7331)}{(z^2 - 1.853z + 0.8633)} \tag{16}$$

To validate the controller and prefilter, the response to a step input is presented in Fig. 14, as well as a Bode magnitude plot to show that $G_\phi(z)$ and $F_\phi(z)$ meet the specifications for all plants in $\boldsymbol{P}$. The dashed line shows the response of the nominal loop transfer function. Not all of the responses meet all specifications, but the controllers are judged to be adequate. Further evaluation of the control laws is described in Sec. V.

Using the closed-loop transfer functions from the bank-angle command-and-hold loop, the heading command-and-hold loop shown in Fig. 15 was designed in a similar manner.

A stability margin of 1.2 was used, and the tracking requirements were a rise time between 3 and 5 s and an overshoot less than 10%. Using these specifications, the controller and prefilter were designed.

$$G_\psi(z) = 0.902 \tag{17a}$$

$$F_\psi(z) = 1 \tag{17b}$$

Because of the robustness designed into the bank-angle command-and-hold loop, the heading command-and-hold loop only required a single gain for adequate performance and robustness.

The localizer tracker control law was developed by closing a loop around the heading command-and-hold loop. Because of the geometry of the localizer, as the aircraft gets closer to the runway, the course deviation becomes more sensitive. To account for this sensitivity, the localizer tracker gain is scheduled with the slant range from the transmitter to prevent the controller from becoming unstable during the approach. The QFT localizer tracker is designed using the

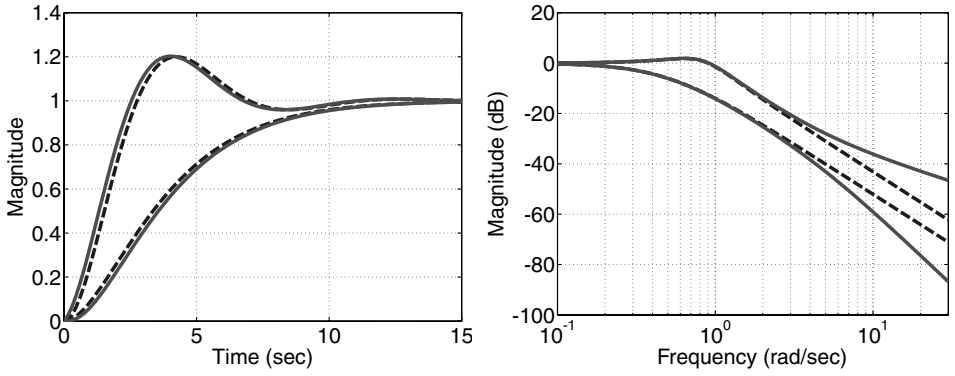

Fig. 10 Bank-angle command-and-hold tracking models.

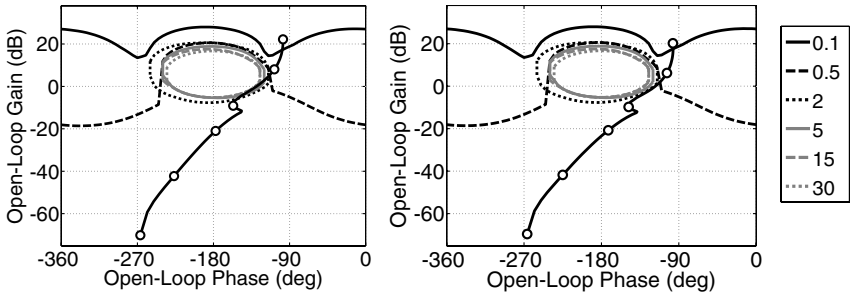

a) Without controller **b) With controller**

Fig. 12 Bank-angle command-and-hold controller synthesis.

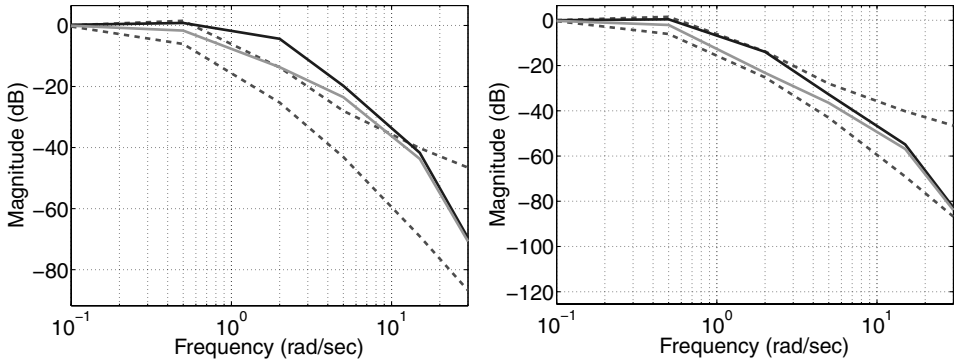

a) Without prefilter **b) With prefilter**

Fig. 13 Bank-angle command-and-hold prefilter synthesis.

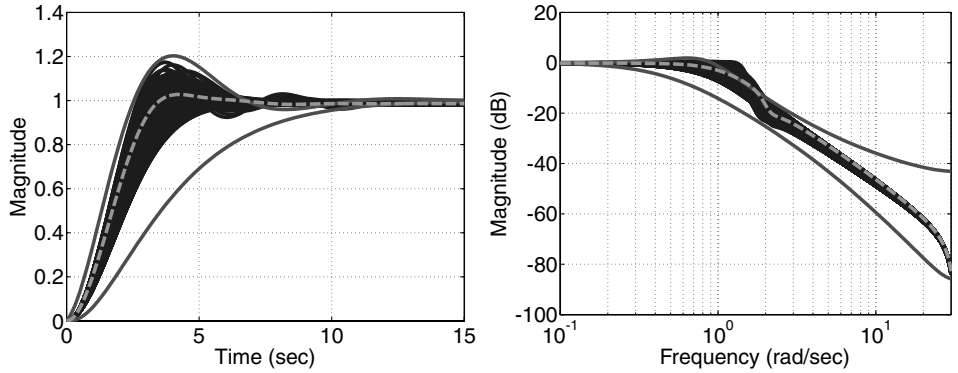

Fig. 14 Bank-angle command-and-hold responses.

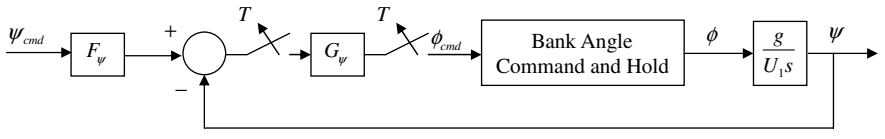

Fig. 15 QFT heading command-and-hold block diagram.

closed-loop heading command-and-hold transfer functions as inner loops (Fig. 16).

Because the desired localizer deviation is zero, thereby making the reference input zero, a prefilter is not needed and so tracking bounds are not included in the design. The localizer tracker loop controller is Eq. (18).

$$G_{\text{loc}}(z) = \frac{0.001268(z - 0.9891)}{(z - 0.9766)} \tag{18}$$

The sigma-Bode plot of Fig. 17 is used to analyze the robustness of the QFT controller. As seen from the figure, the localizer tracker does

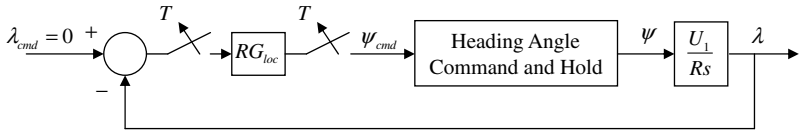

Fig. 16 QFT localizer tracker block diagram.

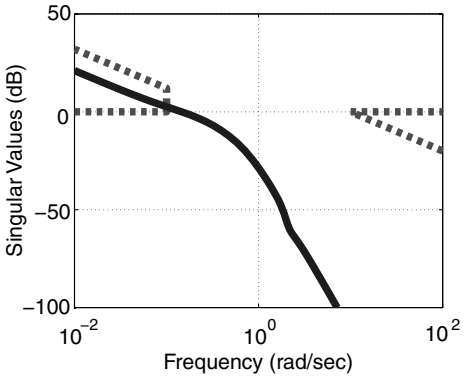

Fig. 17 Localizer sigma-Bode plot.

not completely meet the disturbance rejection requirement. The effect of not meeting this requirement will be analyzed further through simulation in Sec. V.

2. *Longitudinal QFT Controller*

The longitudinal controller consists of a glideslope tracker, automatic flare control law, and airspeed command-and-hold control law. The glideslope tracker and autoflare loops are closed around the pitch-angle command-and-hold loop. The automatic flare control law closes an additional loop around the pitch command-and-hold loop and is engaged upon reaching flare height. After transition from the glideslope tracker controller to the automatic flare controller, the trajectory described in Sec. II is followed to the runway. An airspeed command-and-hold capability is critical for the autoland system and is used to prevent stall in close proximity to the ground. Additionally, if airspeed is excessive during the approach phase, the aircraft can have problems tracking the glideslope, producing an overspeed landing in which the aircraft floats down the runway and lands far downrange. For this work, airspeed is regulated using throttle with both rate and position feedback of the velocity. The airspeed command-and-hold loop involves a single loop closure, which contains the aircraft engine dynamics and throttle as the control.

The longitudinal QFT controller is designed using the same procedure followed for the lateral/directional QFT controller. Unlike a standard PI controller, the QFT design synthesized here does not include a pitch damper inner loop, because it was subsequently determined to be unnecessary for this design. The airspeed command-and-hold loop is designed using the QFT methodology, independent of the pitch-angle command-and-hold loop. A stability margin of 1.2 and tracking requirements of a rise time between 3 and 5 s and an overshoot less than 20% were used for the controller synthesis. Following the QFT design procedure, the pitch-angle command-and-hold controller and prefilter (Fig. 18) were designed as Eq. (19).

$$G_\theta(z) = \frac{0.85254(z - 0.9581)(z - 0.9546)}{(z - 1)(z - 0.7762)} \tag{19a}$$

$$F_\theta(z) = \frac{0.18902(z - 0.5434)}{(z - 0.9128)} \tag{19b}$$

Using the pitch command-and-hold loop as the inner loop, the glideslope tracker is designed in a similar manner. Like the localizer tracker, the glideslope tracker is a regulator, because it is desired for the glideslope deviation to approach zero (Fig. 19). Tracking bounds and a prefilter are not included in the design of the glideslope tracker, because the reference input is zero, and the control laws are scheduled with a range to prevent instability as the aircraft approaches the runway.

The stability margin was chosen to be 1.2, leading to the same gain and phase margin as the pitch attitude command-and-hold loop. Equation (20) is the glideslope tracker controller.

$$G_{\text{gs}}(z) = \frac{0.074231(z - 0.9929)(z - 0.9803)}{z(z - 1)} \tag{20}$$

Figure 20 is the sigma-Bode plot for the glideslope tracker and shows that all requirements are met except for the disturbance rejection requirement. The effect of not meeting the disturbance rejection specification will be evaluated further using a simulation in Sec. V.

The automatic flare loop [Fig. 21] uses the same inner loop as the glideslope tracker. Because of ground effect and the uncertainty associated with it, a stability margin of 1.1 is used, producing a gain

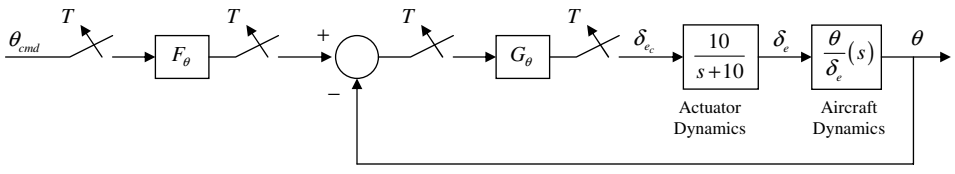

Fig. 18 QFT pitch-angle command-and-hold block diagram.

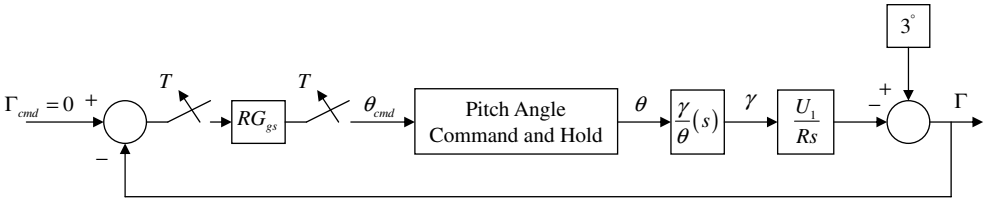

Fig. 19 QFT glideslope tracker block diagram.

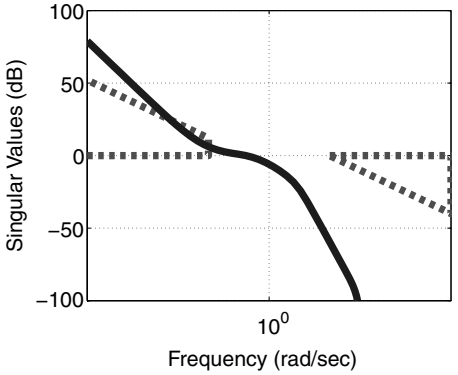

Fig. 20 Glideslope tracker sigma-Bode plot.

margin of 5.6 dB and a phase margin of 54.1 deg using Eq. (14). The tracking specifications used for the autoflare loop were a rise time between 5 and 7 s and an overshoot less than 10%.

Using the tracking bounds and stability bounds, the controller and prefilter were designed as Eq. (21).

$$G_F(z) = \frac{0.0769(z-0.9376)(z-0.8733)}{z(z-1)} \tag{21a}$$

$$F_F(z) = \frac{0.0799(z^2-1.746z+0.775)}{z^2-1.932z+0.935} \tag{21b}$$

Figure 22 displays the sigma-Bode plot for the automatic flare control loop and shows that the autoflare control law designed with QFT meets the specifications.

The airspeed command-and-hold loop is designed in a similar manner as the pitch command-and-hold loop. A stability margin of 1.2 is used, and the tracking requirements are a rise time between 13 and 20 s and an overshoot less than 10%. Using the tracking bounds and stability bounds, the controller was designed as shown in Eq. (22). A prefilter was not needed for the airspeed command-and-hold loop.

$$G_A(z) = \frac{3.988(z-0.972)(z-0.938)}{(z-1)(z-0.7803)} \tag{22}$$

Using the designed controller, the closed-loop gain margin was found to be 27.9 dB and the closed-loop phase margin was found to be 98.7 deg, both of which meet the specifications. In summary, the QFT controller will provide adequate performance and robustness for approach and landing.

B. Proportional–Integral Controllers

Classical z-plane root locus design with sequential loop closures was used to design each of the PI controllers, as detailed next.

1. *Lateral/Directional Proportional–Integral Controller*

The bank-angle command-and-hold loop was designed using a proportional gain of 0.6, which provides a GM of 27.6 dB and a PM of 67.4 deg. Using a proportional gain of 1.1, the heading command-and-hold loop was designed with $GM = 15.3$ dB and $PM = 68.2$ deg. For the localizer control law, the scheduled gain was selected to be 0.0003 and the proportional gain is 1.0. Integral gain is not needed, except when crosswinds are present. The selected

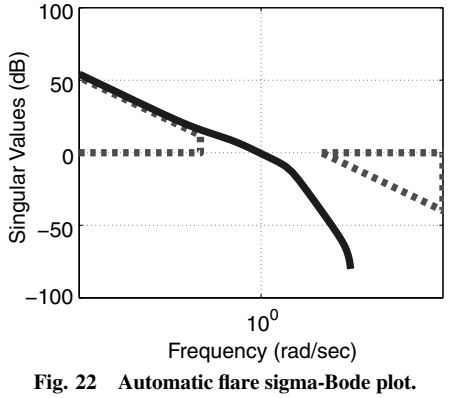

Fig. 22 Automatic flare sigma-Bode plot.

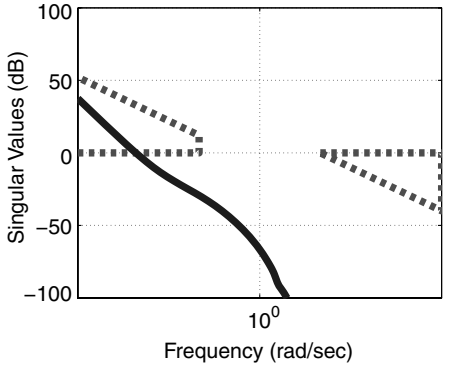

Fig. 23 Localizer tracker sigma-Bode plot.

gains result in $GM = 43.5$ dB and $PM = 20.9$ deg. Although the phase margin is lower than the specifications, modifying the gains produced poor performance, and the originally selected gains are used. The sigma-Bode plot of Fig. 23 shows that the closed-loop system meets the high-frequency specifications but does not meet the low-frequency specifications, because it violates the dashed boundary. Because the selected gains give good performance, the effect of not meeting the low-frequency specifications will be analyzed further using a simulation in Sec. V.

2. *Longitudinal Proportional–Integral Controller*

The pitch damper was designed using a proportional gain of 0.164, which results in $GM = 28.4$ dB and $PM = \infty$ deg. The pitch command-and-hold loop uses a proportional gain of 0.252 and a lead–lag filter with a lead constant of 0.983 and a lag constant of 0.0136. This compensation produces $GM = 33.1$ dB and $PM = 69.6$ deg. Similar to the geometry of the localizer tracker, the glideslope deviation becomes more sensitive as the aircraft approaches the transmitter, and so the tracker gain is scheduled with a slant range to prevent instability. The glideslope scheduled gain was determined to be 0.003, the glideslope proportional gain was 1.0, and the glideslope integral gain was 0.01. These gains lead to $GM = 24.9$ dB and $PM = 8.62$ deg. The low phase margin is judged to be acceptable because the selected gains give good performance for the glideslope tracker. The sigma-Bode plot of Fig. 24 shows that the glideslope tracker satisfies the high-frequency requirements but not the low-frequency requirements. The selected gains will be used

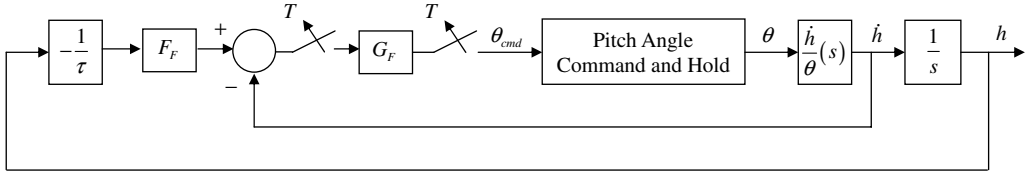

Fig. 21 QFT automatic flare block diagram.

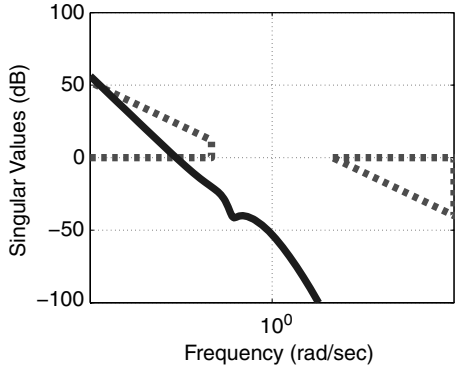

Fig. 24 Glideslope tracker sigma-Bode plot.

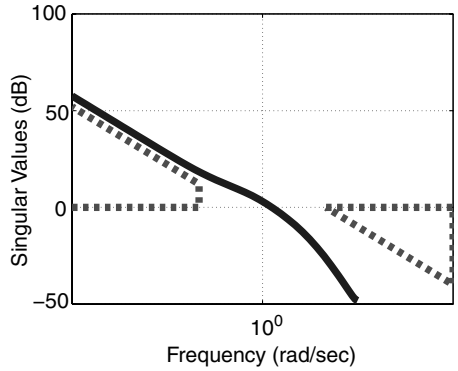

Fig. 25 Autoflare sigma-Bode plot.

because they provide good performance, and the robustness will be analyzed further through simulations.

For the automatic flare loop, gains are selected to minimize touchdown velocity and rollout distance. The automatic flare controller uses a proportional gain of 7.0 and a lead–lag filter with a lead constant of 0.91 and lag constant of 0.0697. This produces a gain margin of 18.7 dB and phase margin of 69.7 deg. The sigma-Bode plot of Fig. 25 shows that the autoflare control law meets both the low- and high-frequency specifications. As with the glideslope and localizer tracker loops, the robustness of the autoflare loop will be analyzed further in Sec. V.

For airspeed command and hold, gains were selected so that the throttle position remains between idle (0%) and full power (100%), with a throttle rate of less than $\pm 10\%/\mathrm{s}$. The proportional gain was determined to be 0.025, integral gain was 1.0, airspeed feedback gain was 1.0, and acceleration feedback gain was 5.0. These gains produce a GM of 21.3 dB and a PM of 59.6 deg.

V. Simulation Results

This section compares the QFT controller to the PI controller for the localizer, glideslope, and automatic flare control laws using linear non-real-time simulation. For this work, *good performance* is defined as meeting the specifications for the nominal plant, and *good performance robustness* is defined as meeting the specifications with model uncertainties or turbulence present. For the test scenario, the airplane is initially placed outside of the maximum deviation of the localizer on a heading that provides a 45-deg intercept angle, 6 n mile from the runway, and flying straight and level at an altitude below the glideslope. The initial airspeed is the approach airspeed of 90 kt (151.90 ft/s) and is maintained throughout the approach until reaching the flare maneuver. After intercepting the glideslope at a range of 4 n mile, it is tracked until the flare height. After reaching the flare height, the throttle is reduced and the flare maneuver is executed. A 6-n-mile localizer intercept and 4-n-mile glideslope intercept represents a worst-case approach, because this is the closest

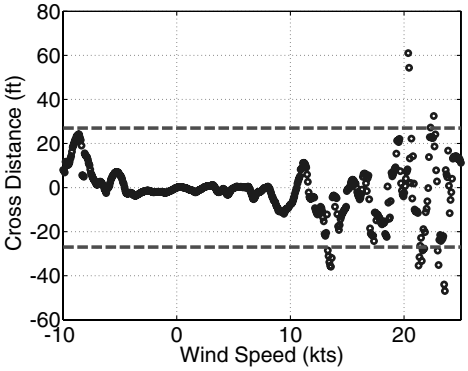

Fig. 26 QFT localizer tracker simulation results for the nominal model plus turbulence for 500 Monte Carlo runs.

to the runway that a localizer and glideslope interception would take place. Winds are aligned with the runway because airplanes typically land into the wind. Crosswind landings, although important, are beyond the scope of this work. The 2σ deviations for each specification used are 1) a localizer cross distance d_{cross} less than 27 ft; 2) a glideslope altitude error ALT_{error} less than 5 ft; 3) an autoflare vertical speed at touchdown, VS_{TD}, greater than -6 ft/s for soft landing and greater than -10 ft/s for hard landing; 4) an autoflare flare distance traveled, d_{flare}, less than 1500 ft; 5) an autoflare aircraft speed at touchdown, V_{TD}, greater than stall speed (114.77 ft/s); and 6) an autoflare aircraft pitch attitude angle, θ_{TD}, greater than -2 deg

A. Localizer Tracker Results

Nominal plant simulations are presented for both still and turbulent air, as defined in [26], and moderate turbulence is assumed to be the worst turbulence encountered. Two Monte Carlo simulations are used, and the QFT localizer tracker is simulated in the same manner as the PI controller, using the same initial conditions. The first simulation tests performance robustness to turbulence, and the second simulation tests performance robustness to the model uncertainties defined in Sec. III. The nominal plant is simulated for 500 samples of uniformly distributed wind values, ranging from a 10-kt tailwind to a 25-kt headwind. The 2σ cross distance from the runway centerline at touchdown should be less than 27 ft, as defined in [26].

1. *Quantitative Feedback Theory*

The nominal plant response of the localizer tracker controller easily intercepted and tracked the localizer without exceeding control position limits or rates, in both still and turbulent air. Figure 26 displays results from the turbulence Monte Carlo simulation. The dashed lines show the cross distance required to meet the specifications of [26]. Of the simulations conducted, 96.2% met the specifications for cross distance, and the average cross distance was -1.33 ft with a standard deviation of 11.05 ft. This performance meets the specifications for localizer cross distance, indicating that the QFT localizer loop is robust to turbulence.

Robustness to model uncertainty is tested for both still and turbulent air using the model uncertainties described in Sec. III. The still-air model-uncertainty Monte Carlo simulations resulted in a cross distance of less than 27 ft, with an average cross distance and standard deviation of less than 1 in. each. When tested in turbulent air, the simulations show that 70% of the cases result in a cross distance less than 27 ft, with an average cross distance of -15.4 ft and a standard deviation of 31.9 ft.

2. *Proportional–Integral Controller*

The PI controller was found to intercept the localizer and track it to the runway with good performance in both still and turbulent air, while keeping control positions and rates within specifications. Figure 27 displays the cross distance at touchdown for each wind

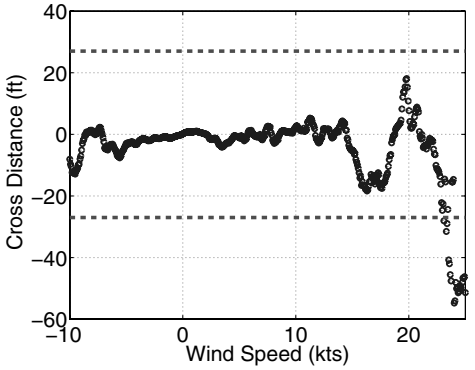

Fig. 27 PI localizer tracker simulation results for the nominal model plus turbulence for 500 Monte Carlo runs.

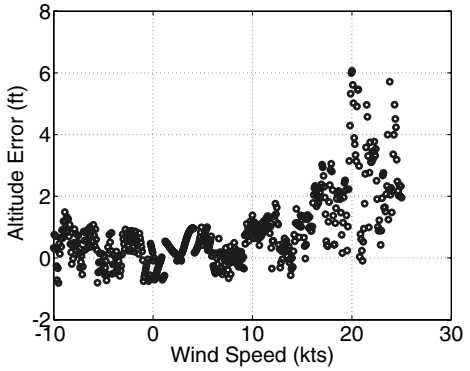

Fig. 28 QFT glideslope tracker simulation results for the nominal model plus turbulence for 500 Monte Carlo runs.

speed tested. The average cross distance is −4.35 ft, with a standard deviation of 10.83 ft, which meets the specifications. Based on these results, the PI localizer control laws are judged to be robust with respect to turbulence.

The evaluation of model uncertainty demonstrated that in still air, the PI controller produced landings within 27 ft of the runway centerline in 100% of the cases, with an average cross distance of 0.212 ft and a standard deviation of 0.03 ft. Yet when moderate turbulence was introduced, landings were within specifications only 14% of the time, with an average cross distance of 0.62 ft and a standard deviation of 120.6 ft. This clearly shows that the PI control laws are robust in still air, but not in turbulent air. Table 4 compares the statistics from the turbulence Monte Carlo simulations for both the QFT and PI controllers. Except for the average cross distance, the performance of each controller is essentially identical.

Table 5 compares statistics from the model uncertainty plus turbulence Monte Carlo simulations. In still air, both controllers provide good performance robustness to model uncertainties. In turbulent air, the QFT controller is seen to produce significantly better performance robustness than the PI controller in all categories.

B. Glideslope Tracker Results

The Monte Carlo simulation for glideslope tracking used 500 simulation runs. According to [26], the glideslope control laws should maintain the aircraft within 12 ft of the glideslope centerline to a distance of 100 ft above the ground. Because the glideslope tracker is used to a distance of approximately 20 ft above the ground, the glideslope tracking requirement is decreased to a 2σ altitude error within ± 5 ft of the glideslope centerline. Performance is evaluated by plotting altitude error (defined here as the difference between the altitude when the flare should start and the actual flare height) versus wind speed.

Table 4 Localizer controller nominal plant turbulence comparison

Performance metric	QFT	PI
Percent successful	96.2	95.6
d_{cross} average, ft	−1.33	−4.35
d_{cross} standard deviation, ft	11.05	10.83

Table 5 Localizer controller model uncertainty robustness comparison, with and without turbulence

Performance metric	Still air		Turbulence	
	QFT	PI	QFT	PI
Percent successful	100	100	69.8	14.0
d_{cross} average, ft	0.21	0.21	−15.4	0.62
d_{cross} standard deviation, ft	0.03	0.03	31.9	120.6

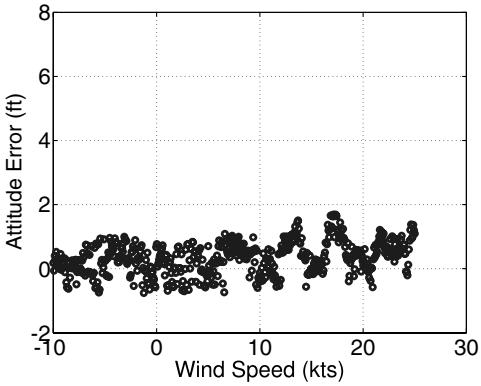

Fig. 29 PI glideslope tracker simulation results for the nominal model plus turbulence for 500 Monte Carlo runs.

1. *Quantitative Feedback Theory*

The QFT glideslope control laws were found to provide good performance and met the specifications for the nominal plant in both the still- and turbulent-air cases. Figure 28 shows that the glideslope tracker meets the specifications for glideslope tracking 98.4% of the time, with a mean altitude error of 0.88 ft and a standard deviation of 1.22 ft. These results show good performance robustness to turbulence for the nominal plant.

The model uncertainty simulations demonstrate that all still-air test cases meet the 5-ft altitude error specification, with an average error of 0.1 ft and a standard deviation of 0.3 ft. When tested in turbulent air, the glideslope controller results in a successful approach to within 5-ft altitude error 88% of the time. The average altitude error was 2.2 ft, with a standard deviation of 2.1 ft. As the turbulence increases, performance robustness to model uncertainty decreases, butthe controller still provides an acceptable level.

2. *Proportional–Integral Glideslope Tracker*

The PI glideslope tracker was found to perform well for both the still- and turbulent-air cases, with essentially identical performance to the QFT glideslope tracker. Turbulence robustness results for the glideslope tracker (Fig. 29) show that the altitude error is less than 1 ft for all cases, with an average altitude error of 0.5 ft and a standard deviation of 0.73 ft. This result shows good performance robustness with respect to turbulence.

The model uncertainty robustness simulations show a 100% success rate, with an average altitude error of −0.211 ft and a standard deviation of 0.138 ft in still air. However, when tested with turbulent air, the PI glideslope control law resulted in a successful approach for only 42% of the cases, with an average altitude error of 8.3 ft and a standard deviation of 5.6 ft. Based on these results, the PI glideslope control law is judged to be robust to model uncertainties in

Table 6 Glideslope controller nominal plant turbulence comparison

Performance metric	QFT	PI
Percent successful	98.4	100
ALT_{error} average, ft	0.88	0.5
ALT_{error} standard deviation, ft	1.22	0.73

Table 7 Glideslope controller model uncertainty robustness comparison, with and without turbulence

Performance metric	Still air		Turbulence	
	QFT	PI	QFT	PI
Percent successful	100	100	88.0	41.7
ALT_{error} average, ft	0.098	-0.21	2.2	8.3
ALT_{error} standard deviation, ft	0.30	0.14	2.1	5.6

still air, but not in turbulent air. In summary, Table 6 compares the PI and QFT glideslope controllers for the turbulence Monte Carlo simulations. Both controller types offer good performance robustness to turbulence for the nominal plant without model uncertainties.

Results from the model uncertainty Monte Carlo simulations in Table 7 show that both controllers are robust to model uncertainties when in still air. However, in turbulent air, the QFT controller clearly offers better performance robustness to model uncertainties, particularly in terms of the percent of successful landings.

C. Automatic Flare Controller Results

To simulate the autoflare maneuver, the aircraft tracks the glideslope to the flare height of 17.47 ft and then executes the flare. At the flare height, airspeed is commanded to a value just above stall, which is 68 kt (114.77 ft/s) in the landing configuration for the aircraft used. According to [26], total distance traveled during the flare should be less than 1500 ft. Reference [19] states that the vertical velocity at touchdown should be greater than -6 ft/s for a smooth landing. A soft landing is considered to be a vertical speed between 0 and -6 ft/s, hard is between -6 and -10 ft/s, and a damage landing is a vertical speed less than -10 ft/s. For this investigation, each of these specifications are to be met for 2σ.

1. *Quantitative Feedback Theory*

Figure 30 shows that the QFT control laws for autoflare provide good performance and a smooth, safe touchdown for both still- and turbulent-air cases. Although the responses in moderate turbulence are more oscillatory, they are still satisfactory overall, including the elevator rates. The turbulence Monte Carlo simulations are shown in Fig. 31 and reflect 99.6% soft landings. Interestingly, in spite of dispersions in vertical speed of up to 5 ft/s, the average vertical velocity during the automatic flare was -0.52 ft/s, with a standard deviation of 0.91 ft/s. The touchdown velocity exhibited dispersions of up to ± 10 ft/s around the nominal speed of 141 ft/s, yet the standard deviation was only 2.6 ft/s. The average touchdown range was -669 ft, with a standard deviation of 223 ft, and the average pitch attitude angle was 0.1 deg, with a standard deviation of 0.9 deg. In spite of these dispersions above wind speeds of 10 kt, the nominal plant meets the specifications for the Monte Carlo turbulence simulations. The QFT automatic flare control laws are therefore judged to be robust with respect to turbulence for the nominal plant.

The model uncertainty simulations show that the QFT autoflare control laws successfully meet the specifications for all of the cases in still air. The average touchdown vertical velocity was -0.14 ft/s, with a standard deviation of 0.02 ft/s. When turbulence is included, the simulations indicated 97% soft landings, 1% hard landings, and 2% damage landings. The average touchdown vertical velocity was -0.52 ft/s, with a standard deviation of 0.99 ft/s. This result demonstrates good performance robustness to model uncertainties, even in the presence of moderate turbulence.

2. *Proportional–Integral Autoflare Controller*

Figure 32 presents responses of the PI autoflare nominal loop for still- and turbulent-air cases. Like the QFT autoflare controller, without model uncertainty the PI autoflare control law successfully lands the aircraft and meets all requirements for both still- and turbulent-air cases. Although the responses in moderate turbulence are more oscillatory, they are still satisfactory overall. Although still acceptable, the elevator rates are almost double those of the QFT

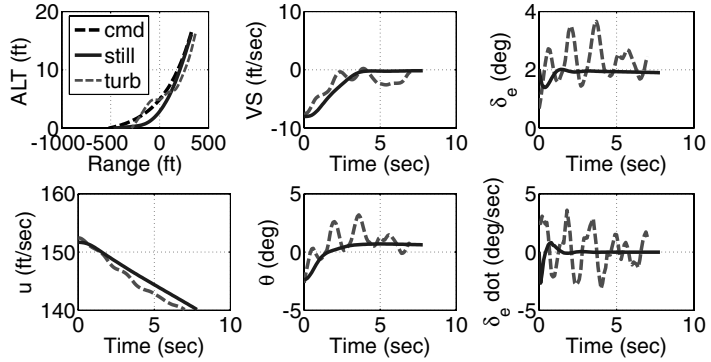

Fig. 30 QFT automatic flare simulation responses for still and turbulent air.

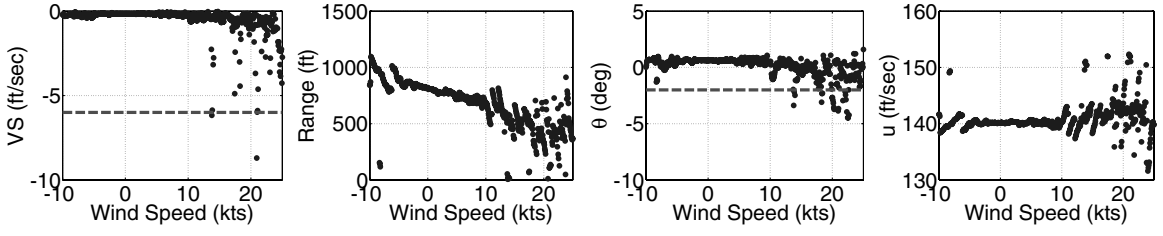

Fig. 31 QFT automatic flare simulation results for the nominal model plus turbulence for 500 Monte Carlo runs.

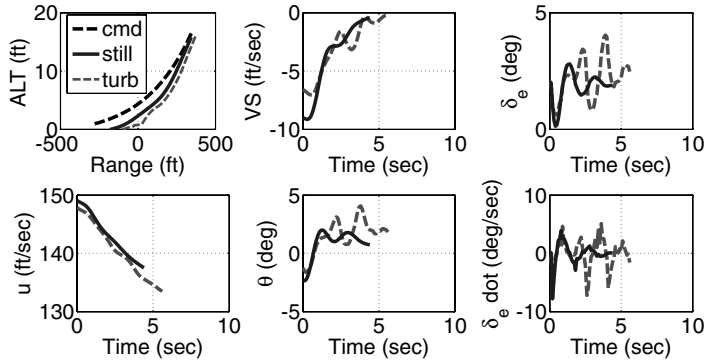

Fig. 32 PI automatic flare simulation responses for still and turbulent air.

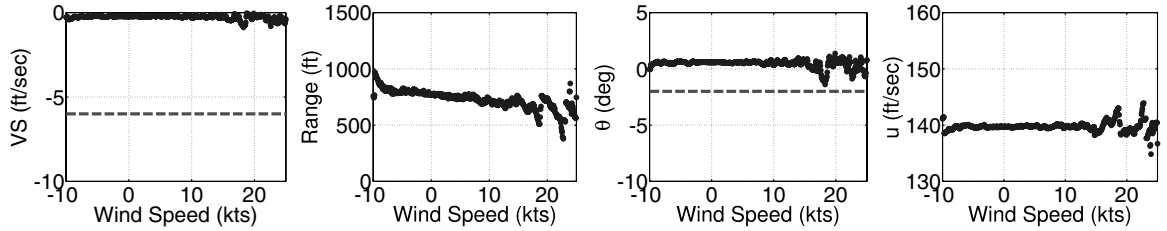

Fig. 33 PI automatic flare simulation results for the nominal model plus turbulence for 500 Monte Carlo runs.

controller. The Monte Carlo simulation for turbulence (Fig. 33) shows that a smooth touchdown is produced in the presence of turbulence for all cases considered. However, the dispersions for wind speeds above 10 kt are seen to be much less than for the QFT autoflare controller. This is borne out by the standard deviations in touchdown vertical velocity (0.13 ft/s), touchdown velocity (0.84 ft/s), touchdown range (82 ft), and pitch attitude angle at touchdown (0.36 deg). These results show that the PI autoflare controller exhibits good performance robustness to turbulence for the nominal plant.

Evaluation of the model uncertainty in still air resulted in 100% successful landings, with an average touchdown vertical speed of -0.73 ft/s and a standard deviation of 0.26 ft/s. However, when tested in turbulent air, only 16% of the cases were soft landings, whereas 16% were hard landings and 67% were damage landings. This result is clearly inferior to the QFT autoflare controller under the same conditions and demonstrates that the PI controller is sensitive to modeling uncertainty in spite of being nearly invariant with respect to turbulence, as shown in Fig. 33. The average vertical speed was -15 ft/s, with a standard deviation of 9.3 ft/s. The average distance traveled during the flare was 109 ft, with a standard deviation of 278 ft. The average pitch attitude angle was -5.4 deg, with a standard deviation of 9.4 deg. The average speed of the aircraft at touchdown was 151.2 ft/s, with a standard deviation of 6.67 ft/s. From these model uncertainty results, it is clear that the PI autoflare control law is robust to model uncertainties in still air, but is not robust to model uncertainties in the presence of moderate turbulence.

Results of the automatic flare controller Monte Carlo simulations for nominal plants with turbulence are summarized in Table 8. For all metrics considered, it is seen that both controller types offer quite similar nominal plant performance robustness to turbulence. Results of the automatic flare Monte Carlo simulations for model uncertainties with turbulence are summarized in Table 9. Although both the PI and QFT controllers exhibit good performance robustness to model uncertainties in still air, it is clear that the QFT controller offers significantly better performance robustness in turbulence when considering landing safety, vertical speed, rollout distance, and pitch attitude angle.

In summary, results for all of the control loops evaluated show that overall, the QFT controllers provide comparable performance to the PI controllers when operating with model uncertainties in still air. The PI control laws provided overall good performance and are robust to turbulence for the nominal plant, but as turbulence increases for a non-nominal plant, robustness degrades significantly. The QFT controllers did not exhibit this characteristic and, by comparison, provided superior robustness when operating with model uncertainties in turbulence, which is the realistic case.

VI. Conclusions

For the localizer, glideslope, and automatic flare controllers, the quantitative feedback theory controller exhibits good performance

Table 8 Autoflare controller nominal plant turbulence comparison

Performance metric	QFT	PI
Percent soft landings	99.6	100
Percent hard landings	0.4	0
Percent damage landings	0	0
VS_{TD} average, ft/s	−0.52	−0.27
VS_{TD} standard deviation, ft/s	0.91	0.12
d_{flare} average, ft	669	728
d_{flare} standard deviation, ft	223	82
θ_{TD} average, deg	0.08	0.45
θ_{TD} standard deviation, deg	0.93	0.36
u_{TD} average, ft/s	141	141
u_{TD} standard deviation, ft/s	2.59	0.84

Table 9 Autoflare controller model uncertainty robustness comparison, with and without turbulence

Performance metric	Still air		Turbulence	
	QFT	PI	QFT	PI
Percent soft landings	100	100	96	16
Percent hard landings	0	0	1	16
Percent damage landings	0	0	2	67
VS_{TD} average, ft/s	−0.14	−0.73	−0.52	−15.3
VS_{TD} standard deviation, ft/s	0.02	0.26	0.99	9.3
d_{flare} average, ft	922	420	669	109
d_{flare} standard deviation, ft	150	57	223	278
θ_{TD} average, deg	0.6	1.65	0.1	−5.4
θ_{TD} standard deviation, deg	0.21	0.06	0.93	9.4
u_{TD} average, ft/s	140	141	145	151
u_{TD} standard deviation, ft/s	0.91	0.95	5.06	6.67

robustness to turbulence for the nominal plant, meeting the specifications 100% of the time in still air and 99.6% of the time for wind speeds from a 10-kt tailwind to a 25-kt headwind. Crosswind landing performance, although important, is beyond the scope of this work. The proportional–integral controller provided similar results for these cases. The quantitative feedback theory and proportional–integral controllers both show good performance robustness to model uncertainties in still air, each meeting the specifications 100% of the time. However, for all of the model uncertainty cases in turbulent air, the quantitative feedback theory controller provides significantly better all-around performance robustness. For the localizer tracker operating with model uncertainty in moderate turbulence, the quantitative feedback theory controller is able to meet the specifications 70% of the time, versus only 14% of the time for the proportional–integral controller. Likewise, the glideslope quantitative feedback theory controller meets the specifications 88% of the time, versus 42% of the time for the proportional–integral controller. For the automatic flare, the quantitative feedback theory controller produced soft landings 97% of the time, versus only 16% of the time for the proportional–integral controller. Based on the results presented in this paper, the quantitative feedback theory controller is judged to offer better overall safety, performance, and robustness for the realistic case of a plant with model uncertainties operating in turbulence conditions.

Appendix: Linear Aircraft Models

Equation (A1) is the Rockwell Commander C700 lateral/directional linear-model power-approach configuration for the flight condition specified in Table 1 [21]. All velocities are in feet per second, all angular quantities are in degrees.

$$\begin{bmatrix} \dot{\beta} \\ \dot{p} \\ \dot{r} \\ \dot{\phi} \end{bmatrix} = \begin{bmatrix} -0.2187 & 0.0319 & -1.0175 & 0.1754 \\ 1.1195 & -2.1647 & 0.1438 & -0.0031 \\ 3.8280 & -0.6813 & -0.2509 & 0.0031 \\ 0.0294 & 0.9225 & -0.0449 & -0.0016 \end{bmatrix} \begin{bmatrix} \beta \\ p \\ r \\ \phi \end{bmatrix} + \begin{bmatrix} 0.0192 & 0.0165 \\ -2.0338 & 0.2634 \\ -0.0209 & -0.7004 \\ -0.1513 & 0.0034 \end{bmatrix} \begin{bmatrix} \delta_a \\ \delta_r \end{bmatrix} \tag{A1}$$

Equation (A2) is the Rockwell Commander C700 longitudinal linear-model power-approach configuration for the flight condition specified in Table 1 [21]. All velocities are in feet per second, all angular quantities are in degrees.

$$\begin{bmatrix} \dot{u} \\ \dot{\alpha} \\ \dot{q} \\ \dot{\theta} \end{bmatrix} = \begin{bmatrix} -0.2371 & -0.3715 & -0.0518 & -0.6304 \\ -0.1394 & -1.0602 & 0.9127 & -0.0230 \\ 0.0918 & 0.2402 & -2.0719 & -0.1316 \\ 0.0129 & 0.0450 & 0.8722 & -0.0080 \end{bmatrix} \begin{bmatrix} u \\ \alpha \\ q \\ \theta \end{bmatrix} + \begin{bmatrix} -0.4012 & 0.1241 \\ -0.6219 & 0.0000 \\ -7.1121 & -0.0036 \\ -0.6369 & 0.0003 \end{bmatrix} \begin{bmatrix} \delta_e \\ \delta_T \end{bmatrix} \tag{A2}$$

References

[1] Stevens, B. L., and Lewis, F. L., *Aircraft Control and Simulation*, Wiley-Interscience, New York, 1992, pp. 338–345.

[2] Blakelock, J. H., *Automatic Control of Aircraft and Missiles*, Wiley-Interscience, New York, 1991, pp. 81–103.

[3] Nho, K., and Agarwal, R. K., "Automatic Landing System Design Using Fuzzy Logic," *Journal of Guidance, Control, and Dynamics*, Vol. 23, No. 2, Feb. 2000, pp. 298–304.

[4] Juang, J.-G., and Chang, W.-B., "Intelligent Automatic Landing System Using Time Delay Neural Network Controller," *Applied Artificial Intelligence*, Vol. 17, No. 7, 2003, pp. 563–581.

[5] Shue, S.-P., and Agarwal, R. K., "Design of Automatic Landing Systems Using Mixed H_2/H_∞ Control," *Journal of Guidance, Control, and Dynamics*, Vol. 22, No. 1, Jan.–Feb. 1999, pp. 103–114.

[6] Kim, D., Choi, Y., and Suk, J., "A Glidepath Tracking Algorithm for Autolanding of a UAV," AIAA Paper 2005-6979, 2005.

[7] Attar, M., Wahnon, E., and Chaimovitz, D., "Advanced Flight Control Technologies for UAVs," 2nd AIAA Unmanned-Unlimited Systems, Technologies, and Operations, San Diego, CA, AIAA Paper 2003-6537, 2003.

[8] Loegering, G., and Harris, S., "Landing Dispersion Results—Global Hawk Auto-Land System," 1st Technical Conference and Workshop on Unmanned Aerospace Vehicles, Portsmouth, VA, AIAA Paper 2002-3457, 2002.

[9] Davidson, R. W., "Flight Control Design and Test of the Joint Unmanned Combat Air System J-UCAS X-45A," 3rd "Unmanned-Unlimited" Technical Conference, Workshop, and Exhibit, Chicago, IL, AIAA Paper 2004-6557, 2004.

[10] Wood, D., "X-47A Pegasus Flight and Mission Systems Design and Test," 2nd Unmanned-Unlimited Systems, Technologies, and Operations, San Diego, CA, AIAA Paper 2003-6628, 2003.

[11] Houpis, C. H., and Rasmussen, S. J., *Quantitative Feedback Theory Fundamentals and Applications*, Marcel Dekker, New York, 1999, p. 19.

[12] Yaniv, O., *Quantitative Feedback Design of Linear and Nonlinear Control Systems*, Kluwer Academic, Norwell, MA, 1999, p. 94.

[13] Horowitz, I., "Application of Quantitative Feedback Theory (QFT) to Flight Control Problems," *Proceedings of the 29th IEEE Conference on Decision and Control*, Vol. 5, Inst. of Electrical and Electronics Engineers, New York, 1990, pp. 2593–2598.

[14] Bossert, D. E., "Design of Robust Quantitative Feedback Theory Controllers for Pitch Attitude Hold Systems," *Journal of Guidance, Control, and Dynamics*, Vol. 17, No. 1, 1994, pp. 217–219.

[15] Wu, S., Grimble, M., and Breslin, S., "Introduction to Quantitative Feedback Theory for Lateral Robust Flight Control Systems Design," *Control Engineering Practice*, Vol. 6, No. 7, July 1998, pp. 805–828.

[16] Sheldon, S. N., and Rasmussen, S. J., "Development and First Successful Flight Test of a QFT Flight Control System," *Proceedings of the IEEE 1994 National Aerospace and Electronics Conference*, Vol. 1, Inst. of Electrical and Electronics Engineers, New York, 1994, pp. 629–636.

[17] Fontenrose, P. L. and C. E. H., Jr., "Development and Flight Testing of Quantitative Feedback Theory Pitch Rate Stability Augmentation System," *Journal of Guidance, Control, and Dynamics*, Vol. 19, No. 5, Sept.–Oct. 1996, pp. 1109–1115.

[18] Anon., "Instrument Flying Handbook," Federal Aviation Administration, FAA-H-9093-15, 2001.

[19] Roskam, J., *Airplane Flight Dynamics and Automatic Flight Controls, Part 2*, DARcorporation, Lawrence, KS, 2003, p. 843.

[20] Valasek, J., and Chen, W., "Observer/Kalman Filter Identification for Online System Identification of Aircraft," *Journal of Guidance, Control, and Dynamics*, Vol. 26, No. 2, Mar.–Apr. 2003, pp. 347–353.

[21] Anon., *Rockwell Commander 700 Pilots Operating Handbook*, Rockwell International, Bethany, OK, 1979.

[22] Lan, C. E., and Roskam, J., *Airplane Aerodynamics and Performance*, Roskam Aviation and Engineering, Ottawa, KS, 1980, pp. 449–450.

[23] Anon., "Military Standard Flying Qualities of Piloted Aircraft," U.S. Dept. of Defense, Rept. MIL-STD-1797a, Mar. 1990.

[24] Roskam, J., *Airplane Flight Dynamics and Automatic Flight Controls, Part 1*, DARcorporation, Lawrence, KS, 2003, p. 176.

[25] Franklin, G., Powell, J. D., and Workman, M. L., *Digital Control of Dynamic Systems*, Addison Wesley Longman, Reading, MA, 1998, p. 163.

[26] Anon., "Flight Control Systems - Design, Installation and Test of Piloted Aircraft, General Specification For," U.S. Dept. of Defense, Rept. MIL-STD-9490D, 1964.

[27] Ridgely, D. B., Banda, S. S., McQuade, T. E., and Lynch, P. J., "Linear-Quadratic-Gaussian With Loop-Transfer-Recovery Methodology for an Unmanned Aircraft," *Journal of Guidance, Control, and Dynamics*, Vol. 10, No. 1, Jan. 1987, pp. 82–89.